Hazard Avoidance for High-Speed Mobile Robots in Rough Terrain

• • • • • • • • • • • • • • • • •   • • • • • • • • • • • •

Matthew Spenko, Yoji Kuroda,
Steven Dubowsky, and Karl Iagnemma
Department of Mechanical Engineering
Massachusetts Institute of Technology
Cambridge, Massachusetts 02139
e-mail: mspenko@alum.mit.edu

Unmanned ground vehicles have important applications in high speed rough terrain scenarios. In these scenarios, unexpected and dangerous situations can occur that require rapid hazard avoidance maneuvers. At high speeds, there is limited time to perform navigation and hazard avoidance calculations based on detailed vehicle and terrain models. This paper presents a method for high speed hazard avoidance based on the "trajectory space," which is a compact model-based representation of a robot's dynamic performance limits in rough, natural terrain. Simulation and experimental results on a small gasoline-powered unmanned ground vehicle demonstrate the method's effectiveness on sloped and rough terrain. © 2006 Wiley Periodicals, Inc.

1. INTRODUCTION AND BACKGROUND LITERATURE

Many important military, disaster relief, search and rescue, and surveillance applications would benefit from an unmanned ground vehicle (UGV) capable of moving safely at high speeds through rough, natural terrain of varying compositions and physical parameters (Gerhart, 1999; Walker, 2001). High-speed UGVs can reach their target location in less time than their low-speed counterparts, increase reconnaissance ef-

fectiveness by traversing more terrain in a fixed amount of time, and spend less time in unsafe situations.

Often a UGV is directed to follow a preplanned route (or navigate among predefined waypoints) generated by an off-line planning algorithm using coarse topographical map data. In natural terrain at high speeds, dangerous situations unforeseen by the high-level planner are likely to occur that require a UGV to quickly execute an emergency maneuver. These may be the result of outdated topographical map data, unidentified hazards due to sensor limitations or errors, or unanticipated physical terrain conditions. Despite ever increasing computing power, at high speeds there is little time to accurately model com-

plex and detailed vehicle/terrain interactions in real time and perform navigation based on these models.

This paper presents a local replanning algorithm for emergency hazard avoidance situations applicable to UGVs traveling at high speed on rough natural terrain. Note that "high speed" is a function of vehicle geometry and terrain and is loosely defined here as speeds that excite vehicle dynamic effects, such as rollover, ballistic motion, sideslip, and wheel slip. The proposed algorithm considers the effects of terrain inclination, roughness, and traction. In addition, it generates dynamically feasible paths by construction and is computationally efficient. The paper does not focus on path following or sensing, although they are recognized as important and necessary components for a comprehensive unmanned ground vehicle.

1.1. Problem Formulation and Key Assumptions

In this paper, a UGV is assumed to be following a nominal (preplanned) path, $\mathbf{x}_{nominal}(s) = (x(s), y(s))$, $s \in [s_0, s_f]$. Associated with $\mathbf{x}_{nominal}$ is a nominal trajectory comprised of a vehicle's desired velocity and path curvature, $\tau_{nominal}(s) = (v(s), \kappa(s))$. There exists a unique mapping from a vehicle's trajectory to its path given the vehicle's initial curvature, heading, and position.

Hazards are defined as discrete objects or terrain features that significantly impede or halt UGV motion, such as trees, boulders, ditches, knolls, and areas of poorly traversable terrain (e.g., water or very soft soil). Hazards are assumed to be detected by on-board range sensors. It is recognized that hazard detection and sensing are important aspects of UGV mobility and an active research topic (Fish, 2003; Shoemaker & Borenstein, 2000); however, it is not a focus of this work.

A terrain patch is described by its average roll (ϕ), pitch (ψ), roughness (ϖ), and traction coefficient (μ). It is assumed that coarse estimates of the tire/ground traction coefficient and ground roughness are known or can be determined online using currently available techniques (Arakawa & Krotkov, 1993; Iagnemma, Kang, Brooks & Dubowsky, 2003; Manduchi, Castano, Talukder & Matthies, 2005).

The vehicle is assumed to be equipped with a forward-looking range sensor that can measure terrain elevation and locate hazards up to several vehicle lengths ahead; an inertial navigation sensor that can measure the vehicle's roll, pitch, yaw, roll rates, pitch rates, yaw rates, and translational accel-

erations with reasonable uncertainty; and a global positioning system that can measure the vehicle's position and velocity in space with reasonable uncertainty.

1.2. Background Literature Review

Hazard avoidance for UGVs has been traditionally performed by selecting from a set of candidate paths (i.e., search techniques over small spaces) or through the use of reactive (reflexive) behaviors. Other proposed methods of interest include potential fields, mixed-integer-linear programming, the curvature-velocity method (Simmons, 1996), and the dynamic window approach (Fox, Burgard & Thrun, 1997). Many of the techniques have been designed for use on flat or slightly rolling terrain at speeds that do not excite the vehicle dynamics. This paper addresses hazard avoidance on flat, rough, and uneven terrain at speeds that excite vehicle dynamics.

Previous researchers have addressed this problem with a search-based technique to navigate a HMMWV-class vehicle at speeds up to 10 m/s while avoiding large hazards (Coombs, Lacaze, Legowik & Murphy, 2000). The method relies on a precomputed database of approximately 1.5×10^7 clothoidal paths. Since the vehicle is assumed to travel on relatively flat terrain at fairly low speeds, the model used in the calculations does not consider vehicle dynamics. An online algorithm eliminates candidate clothoids that intersect with hazards or are not feasible given the initial steering conditions. From the remaining path, the algorithm chooses one that follows the most benign terrain. Several contenders of the 2005 DARPA Grand Challenge utilize similar approaches which have proven to be successful for speeds in excess of 8 m/s. However, the techniques do not consider the important aspects of terrain roughness, inclination, and vehicle/terrain traction characteristics, all of which will become increasingly more important as autonomous vehicles move from traversing roads and relatively benign terrain to more dangerous and extreme topography.

In another successful technique, a UGV uses a voting scheme to evaluate several forward simulated candidate paths through a terrain region (Kelly & Stentz, 1998). An arbitrator chooses the path closest to the goal location that does not impact a hazard. This method has been experimentally demonstrated on a HMMWV-class vehicle at speeds up to 4.5 m/s on natural terrain. This work employs kine-

matic UGV models to evaluate potential paths, and does not account for dynamic vehicle effects, such as rollover and sideslip. An extension of this work proposes to limit the set of initial candidate paths by placing constraints on the space of a vehicle's velocity and curvature (Sanjiv & Kelly, 1996). This is similar in some ways to the method presented in this paper; however, this methodology again does not consider dynamic effects that can be important at high speeds.

Another class of techniques applied to mobile robot navigation in natural terrain relies on reactive behaviors that generate a specific action in response to online sensor signals (Brooks, 1986). A successful reactive behavior technique for outdoor hazard avoidance arbitrates between hazard avoidance and goal seeking and allows for UGV navigation at speeds of up to 1 m/s (Daily *et al.* 1998; Olin & Tseng, 1991). Another approach defined five candidate behaviors that "voted" for or against a set of steering angles: "avoid obstacles," "follow the road," "seek the goal," "maintain heading," and "track the path" (Langer, Rosenblatt & Hebert, 1994). The steering angle with the most votes was then executed. Although both of these techniques have been successful at low to moderate speeds, none explicitly consider vehicle dynamics and terrain characteristics which can result in trajectories that are impossible for a UGV to safely execute at high speeds on rough terrain.

Potential field methods have also been applied to mobile ground robots in natural terrain (Chanclou & Luciani, 1996; Haddad, Khatib, Lacroix & Chatila, 1998). These methods define a potential field in Cartesian space with goal locations corresponding to "sink" functions and hazard locations corresponding to "source" functions. A vehicle then navigates toward points of increasingly low potential. These techniques have proven successful for slow moving UGVs on flat terrain; however, they do not consider the effects of robot dynamics, terrain inclination, roughness, or traction. A potential field method has recently been developed for high speed vehicles on rough terrain that does consider these effects (Shimoda, Kuroda & Iagnemma, 2005). This work utilizes the trajectory space framework presented in this paper.

Two similar approaches of interest are the curvature-velocity method (Simmons, 1996) and the dynamic window technique (Fox, Burgard & Thrun, 1997; Brock & Khatib, 1999; Philippsen & Siegwart, 2003). Both consider the effects of velocity and acceleration constraints on synchro-drive robots operating in indoor environments. A two-dimensional space consisting of a vehicle's translational and rotational velocities is created. Velocity combinations that cannot be reached due to acceleration constraints and obstacle locations are removed from this space. A translational and rotational velocity is then chosen from the space by maximizing an objective function. Both the curvature-velocity method and dynamic window approach have similar elements to the trajectory space method described in this paper. However, they do not consider critical vehicle/terrain interactions, vehicle dynamic effects, or terrain inclination.

In summary, numerous techniques have been developed for navigation and hazard avoidance of UGVs. In general, these techniques do not explicitly consider dynamic vehicle and terrain effects that are important for UGVs traversing rough terrain at high speeds. A method that considers these effects and is computationally tractable is the objective of this work.

2. TRAJECTORY SPACE DESCRIPTION

The hazard avoidance algorithm presented here is based on the trajectory space, defined as the two-dimensional space of a vehicle's instantaneous longitudinal velocity, v, and path curvature, κ (Spenko, Iagnemma & Dubowsky, 2004). A UGV's "position" in the trajectory space is a velocity-curvature pair (v, κ). The relationship of a point in the trajectory space and a vehicle maneuver is illustrated in Figure 1. Velocities are limited to positive values in this work. A transition between two points in the space can be thought of as a simple maneuver.

The trajectory space is a useful space for UGV navigation for two reasons. First, points in the trajectory space easily map to the points in UGV actuation space (generally consisting one throttle/brake control input and one steering angle control input). Thus, navigation algorithms developed for use in the trajectory space will map to command inputs that obey vehicle nonholonomic constraints. Second, constraints related to terrain parameters including inclination, roughness, and traction and to dynamic effects, such as UGV rollover and sideslip are easily expressible in the trajectory space, since these effects are strong functions of velocity and path curvature.
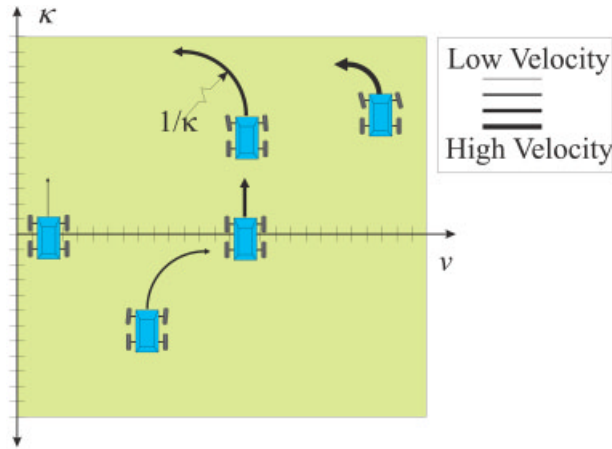
Figure 1. Representation of vehicle action as described by coordinates in the trajectory space.

Sections 2.1 and 2.2 describe computation of these constraints using simple UGV and terrain models. These computationally efficient, low-order models have been shown to sufficiently capture the important vehicle dynamics and vehicle/terrain interactions.

2.1. The Dynamic Trajectory Space

The dynamic trajectory space is a subspace of the trajectory space that consists of velocity-curvature pairs that correspond to dynamically feasible maneuvers on a given terrain patch. Dynamically feasible maneuvers are here defined as maneuvers that do not self-induce vehicle failure due to excessive sideslip (i.e., skidding) or rollover and are physically attainable considering vehicle steering properties.

2.1.1. Sideslip Constraint Computation

Although some sideslip is expected and likely unavoidable, substantial slip that causes large heading or path following errors is detrimental. A constraint function relating UGV velocity and path curvature to lateral traction limits can be derived from the free body diagram shown in Figure 2, assuming $\dot{v}=0$ and $\dot{\kappa}=0$. Here $\{xyz\}$ represents a body-fixed coordinate frame and $\{XYZ\}$ represents an inertial frame.

For simplicity vehicle roll and pitch are assumed to be equal to the roll and pitch of the terrain be-
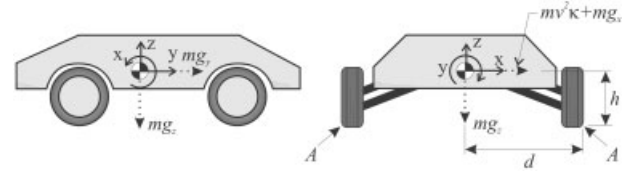
Figure 2. Sideslip vehicle model.

neath the vehicle. Hence, suspension travel is neglected. The vehicle roll (ϕ), pitch (ψ), and yaw (θ) associated transformation matrices are

$$G_\phi = \begin{bmatrix} \cos\phi & 0 & -\sin\phi \\ 0 & 1 & 0 \\ \sin\phi & 0 & \cos\phi \end{bmatrix},$$

$$G_\psi = \begin{bmatrix} 1 & 0 & 0 \\ 0 & \cos\psi & \sin\psi \\ 0 & -\sin\psi & \cos\psi \end{bmatrix},$$

$$G_\theta = \begin{bmatrix} \cos\theta & \sin\theta & 0 \\ -\sin\theta & \cos\theta & 0 \\ 0 & 0 & 1 \end{bmatrix}. \tag{1}$$

The acceleration due to gravity in $\{xyz\}$ following a roll, pitch, yaw transformation is thus: $\mathbf{g_{xyz}} = G_\phi G_\psi G_\theta \mathbf{g_{XYZ}}$, where $\mathbf{g_{xyz}} = [g_x\ g_y\ g_z]^T$. A vehicle begins to skid when the traction force is equal to the sum of the centripetal and gravitational force components. In this simplified analysis, accelerations other than gravity in the z direction are ignored. The predicted maximum curvature before skidding occurs can be computed as

$$\kappa_{\text{slip}}^{\text{min,max}} = \frac{-g_x \pm \mu g_z}{v^2}. \tag{2}$$

The two solutions correspond to downslope/upslope travel. Treating Eq. (2) as a constraint function, the sideslip space is defined as:

Definition 1 (Sideslip Space): *The sideslip space, A, is the set of velocity and curvature pairs that do not induce vehicle sideslip on a given terrain patch:*
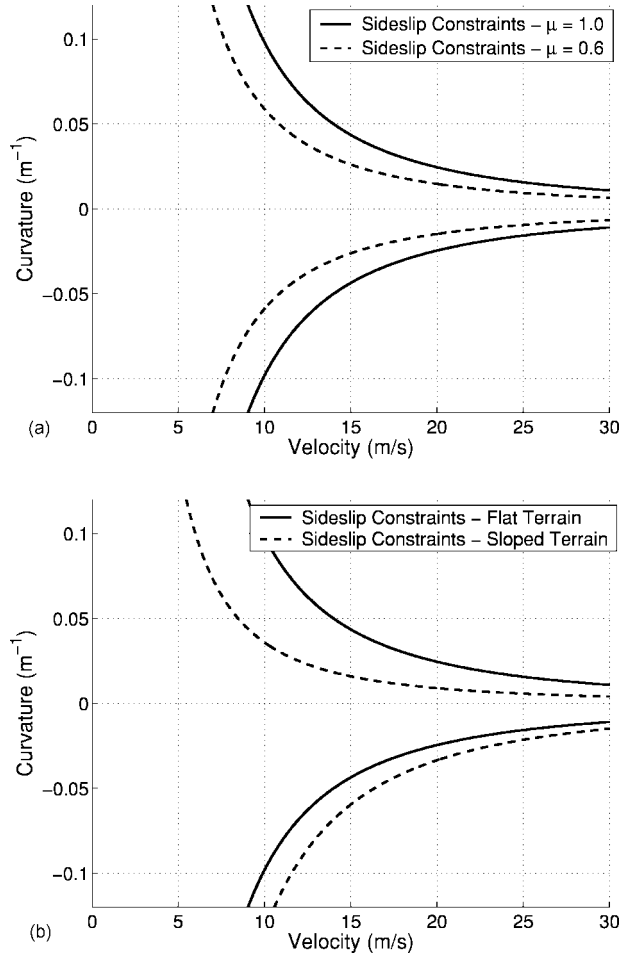
Figure 3. Sideslip constraint comparison for varying (a) traction coefficient and (b) inclination.

$$A(\phi, \psi, \nu, \mu) \equiv \{\forall \kappa | \kappa_{\text{slip}}^{\min} < \kappa < \kappa_{\text{slip}}^{\max}\}. \qquad (3)$$

Figure 3(a) illustrates the variation of the sideslip constraint as a function of traction coefficient. As expected, as the traction coefficient increases (at a fixed speed) a UGV can safely execute maneuvers of increasing curvature. Figure 3(b) illustrates the variation of the sideslip constraint as a function of terrain inclination. The sloped terrain constraint corresponds to a UGV traversing a side slope of 30° with the fall line perpendicular to the vehicle's heading (negative curvatures represent a downslope turn). As expected the UGV can safely execute a downslope turn at higher velocity than it can execute an upslope turn, as a result of the interaction of centripetal acceleration and gravity.

Clearly the sideslip model presented here does not include potentially significant effects such as load transfer; however it is employed due to its simplicity and has shown to be reasonably accurate in practice (Spenko, 2005).

2.1.2. Rollover Constraint Computation

Rollover is generally undesirable despite the fact that some UGVs are designed to be invertible (Walker, 2001). A trajectory space constraint for vehicle rollover can be computed from analytical models of varying complexity. Here a rigid body model is presented, although models that consider the effects of tire stiffness and suspension compliance are also available (Spenko, 2005; Chen & Peng, 1999).

Rollover is initiated when the body force vector expressed at the vehicle center of mass is directed outside the convex polygon formed by the tire/terrain contact points. For a UGV with a wheelbase greater than its track width, this most commonly occurs when the moment about either of the points *A* in Figure 2 is equal to zero. The resulting constraint function for the rollover space is

$$\kappa_{\text{rollover}}^{\max,\min} = \frac{dg_z \pm hg_x}{h\nu^2}, \qquad (4)$$

where *d* is one-half of the axle length, *h* is the center of mass height, and ν is the vehicle's longitudinal velocity. The two solutions correspond to upslope/downslope travel. This model has been found experimentally to accurately predict rollover on flat, smooth terrain (Spenko, 2005). The effect of terrain roughness of the accuracy of this model is investigated in Section 2.3.

Definition 2 (Rollover Space): *The rollover space, B, is the set of velocity and curvature pairs on a given terrain patch that do not induce vehicle rollover:*

$$B(\phi, \psi, \nu) \equiv \{\forall \kappa | \kappa_{\text{rollover}}^{\min} < \kappa < \kappa_{\text{rollover}}^{\max}\}. \qquad (5)$$

Similar to Figure 3(b), the rollover constraint will vary as a function of terrain inclination.

2.1.3. Steering Constraint Computation

Steering constraints describe the limitations imposed by a UGV's kinematic steering and handling properties on its attainable maneuvers. Here, front-steered
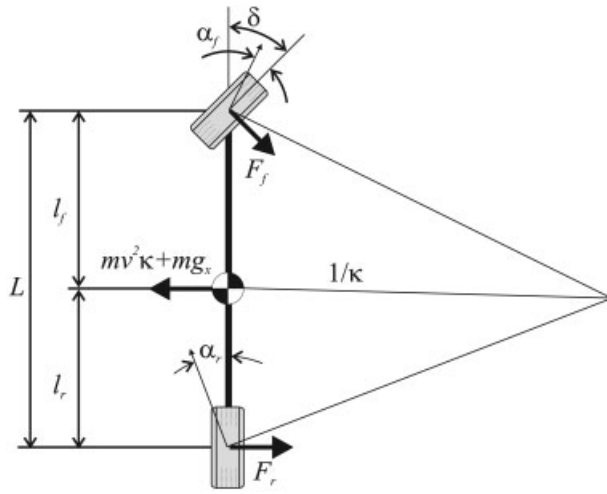
Figure 4. Single-track vehicle model for steering mechanism limit computation (adapted from Gillespie, 1992).

Figure 5. Illustration of comparison of steering limits for over/understeered vehicles.

vehicles that can exhibit neutral-, over-, or understeer are considered. Many factors contribute to determining if a vehicle will exhibit oversteer or understeer (Gillespie, 1992). Tire cornering properties and the location of the center of mass are major influences, and their effects are investigated here.

The slip angle, α, is the angle between the heading direction of the tire and the direction of travel (see Figure 4). At low slip angles (typically $\alpha < 5°$), the relationship between the cornering force and slip angles is approximately linear (Gillespie, 1992):

$$F_{f,r} = C_k \alpha_{f,r}, \qquad (6)$$

where C_k is the cornering stiffness of the tire. Summing the lateral forces acting on the vehicle results in

$$F_f \cos \delta + F_r = m v^2 \kappa \pm m g_x. \qquad (7)$$

Summing the moments about the center of mass yields

$$F_f l_f \cos \delta = F_r l_r. \qquad (8)$$

Combining Eqs. (6)–(8) and linearizing about $\delta = 0$ yields

$$\alpha_{f,r} = \frac{m(v^2 \kappa \pm g_x)}{C_k \left(1 + \dfrac{l_{f,r}}{l_{r,f}} \right)}. \qquad (9)$$

By examining Figure 4, it is evident that

$$\delta = L \kappa + \alpha_f - \alpha_r. \qquad (10)$$

Combining Eqs. (9) and (10) and yields a constraint function for the steering space:

$$\kappa_{\text{steering}}^{\text{min,max}} = \frac{C_k L \delta_{\max} \pm m g_x (l_f - l_r)}{C_k L^2 + m v^2 (l_r - l_f)}. \qquad (11)$$

Definition 3 (Steering Space): *The steering space, C, is the set of velocity and curvature pairs that are attainable given a vehicle's kinematic configuration and tire parameters:*

$$C(\phi, \psi, \mu, v, m, C_k, l_{f,r}) \equiv \{ \forall \kappa \,|\, \kappa_{\text{steering}}^{\text{min}} < \kappa < \kappa_{\text{steering}}^{\text{max}} \}. \qquad (12)$$

Figure 5 illustrates the difference in steering constraints for generic understeered and oversteered vehicles.
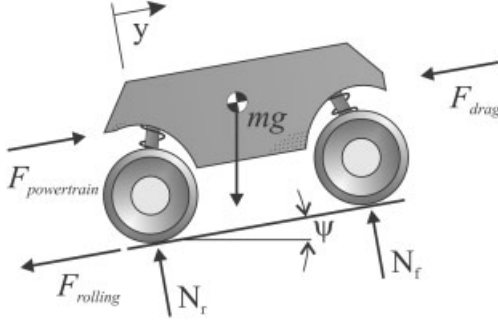
Figure 6. Simple drive train vehicle model.

2.1.4. Drive Train Constraint Computation

Generally a UGV's maximum forward velocity is a function of the drive train characteristics, rolling resistance, aerodynamic drag effects, and terrain inclination. Here a trajectory space constraint related to maximum forward velocity is computed from the model in Figure 6.

For this system, summing the forces in the y direction yields

$$m\ddot{y} = F_{\text{powertrain}} - F_{\text{drag}} - F_{\text{rolling}} - mg \sin \varphi. \quad (13)$$

A model of the force generated by a general UGV power train can be written as

$$F_{\text{powertrain}} = \frac{T(\nu)G}{r}, \quad (14)$$

where $T(\nu)$ is the torque, G is the transmission ratio, and r is the wheel radius. The aerodynamic drag force on a vehicle can be modeled by the relation (White, 1994)

$$F_{\text{drag}} = \frac{1}{2}\rho A_r C_d (\nu)^2, \quad (15)$$

where ρ is the density of air, A_r is the reference area of the vehicle, and C_d is the drag coefficient. The rolling resistance acting on a wheeled vehicle can be modeled by the relation (Beer & Johnston, 1988)

$$F_{\text{rolling}} = C_{rr}mg \cos \varphi, \quad (16)$$

where C_{rr} is the coefficient of rolling resistance. Combining Eqs. (15) and (16) and setting $\ddot{y}=0$ yields the maximum vehicle forward velocity, which can be treated as a constraint function on the drive train space:

$$\nu_{\max} = \sqrt{\frac{2(T(\nu)G - rC_{rr}mg \cos \varphi - rmg \sin \varphi)}{r\rho C_d}}. \quad (17)$$

Definition 4 (Drive Train Space): *The drive train space, D, is the set of velocity and curvature pairs that are attainable on a given terrain patch given a vehicle's drive train and aerodynamic properties*:

$$D(\phi,\psi,\varpi,\mu,\kappa) \equiv \{\forall \nu | 0 \leq \nu \leq \nu_{\max}\}, \quad (18)$$

where ν_{max} is the maximum vehicle velocity.

The sideslip space, rollover space, steering space, and drive train space are subspaces of the trajectory space constrained by various functions related to UGV mobility. Together they comprise the dynamic trajectory space.

Definition 5 (Dynamic Trajectory Space): *The dynamic trajectory space, Γ, is the set of velocity and curvature pairs that are attainable on a given terrain patch given a vehicle's dynamic, steering, and drive train properties:*

$$\Gamma \equiv A \cap B \cap C \cap D. \quad (19)$$

Figure 7 shows an illustration of the dynamic trajectory space. The dynamic trajectory space represents all kinematically and dynamically feasible velocity-curvature pairs for a particular vehicle on a particular terrain patch.

2.2. The Hazard Trajectory Space

In Section 2.1, models were presented for computing trajectory space constraints that limit the space of maneuvers that are safely attainable on a given terrain patch at a given instant. Physical hazards (such as large rocks, trees, deep water, etc.) also limit the space of safely attainable maneuvers.

Hazards can be generally classified as belonging to one of two types: Trajectory independent hazards
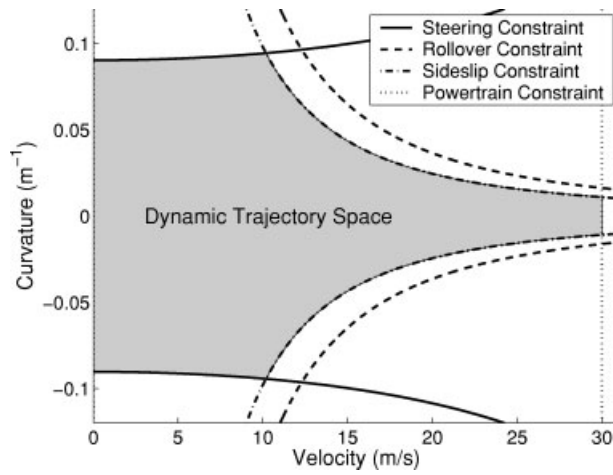
Figure 7. Dynamic trajectory space (shaded region) illustration for an oversteered vehicle on flat terrain.

and trajectory dependent hazards. A trajectory independent hazard, such as a large tree, boulder, or water trap, is one that a vehicle cannot safely travel across, over, or through independent of approach velocity and direction. A trajectory dependent hazard is one where safe traversal depends on the vehicle approach velocity and/or direction, such as a shallow ditch where at high velocities a UGV may be able to achieve ballistic motion and successfully "jump" the ditch.

The hazard trajectory space is defined as the space of velocity-curvature pairs that, at the current UGV position, would result in a collision between the vehicle and hazard. For a trajectory independent hazard, curvatures between $\kappa_{\text{hazard}}^{\max}$ and $\kappa_{\text{hazard}}^{\min}$ in Figure 8 would thus belong to the hazard trajectory space. The minimum and maximum curvatures associated with a hazard, $\kappa_{\text{hazard}}^{\max}$ and $\kappa_{\text{hazard}}^{\min}$, are generally functions of a vehicle's velocity due to the fact that vehicles follow clothoidal paths, which correspond to the steering angle changing with constant velocity, when transitioning between curvatures (Spenko, 2005). An illustration of the hazard trajectory space for a trajectory independent hazard is shown in Figure 9(a). An illustration of the hazard trajectory space for a trajectory dependent hazard is shown in Figure 9(b).

Definition 6 (Hazard Trajectory Space): *The hazard trajectory space, Ω, consists of curvatures and veloci-*
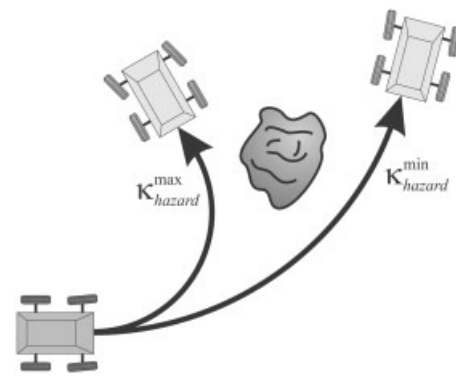
Figure 8. Illustration of maximum and minimum curvatures necessary to avoid impact with a hazard.

ties that, if maintained from the current vehicle position, would lead to intersection with a hazard.

$$\Omega(\varpi) \equiv \{\forall (\nu, \kappa) | \nu_{\text{hazard}}^{\min} \leqslant \nu \leqslant \nu_{\text{hazard}}^{\max}, \kappa_{\text{hazard}}^{\min} \leqslant \kappa$$
$$\leqslant \kappa_{\text{hazard}}^{\max}\}. \qquad (20)$$

Note that there are no limitations as to the number of hazards that can appear in the trajectory space. The hazard trajectory space is generated by evaluating a precomputed library of clothoidal paths that connect the current location in the trajectory space to other locations.

2.3. Effect of Roughness on Trajectory Space Constraints

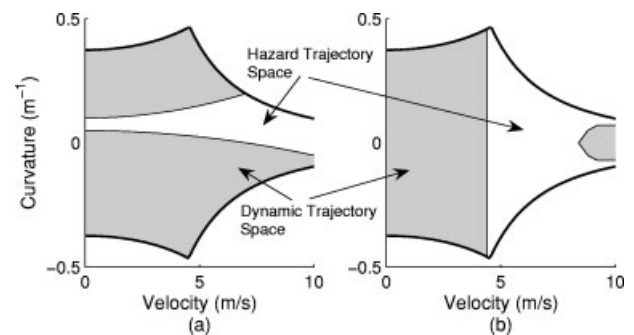The above models of UGV mobility have assumed that the terrain is smooth. Terrain roughness influ-

Figure 9. Illustration of hazard trajectory space for: (a) Trajectory independent hazard and (b) trajectory dependent hazard.
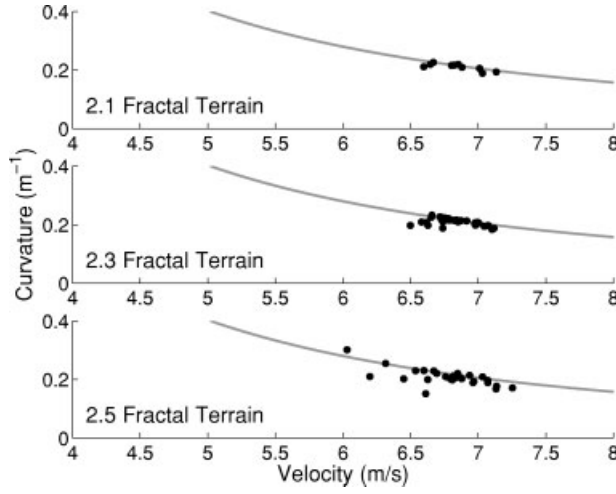
Figure 10. Comparison of rollover constraints on smooth and rough terrain.

ences UGV mobility by inducing variation in the wheel normal forces, which affects cornering and stability properties. The effect of terrain roughness on UGV sideslip and rollover has been studied in simulation (Spenko, 2005). Representative results for an analysis of UGV rollover are shown in Figure 10.

It can be observed that as terrain roughness increases (represented by an increasing fractal number), the variation in velocity and curvature at which rollover is initiated increases. In general, terrain roughness tends to induce variation in the location of trajectory space constraints. Based on this observation, researchers have suggested that a probabilistic representation of vehicle mobility is a more useful analysis tool than a deterministic (i.e., "go/no-go") analysis (Golda, 2003). A more thorough discussion of the effect of terrain roughness on trajectory space constraints can be found in Spenko (2005).

2.4. The Admissible Trajectory Space

Not all points in the trajectory space can be reached, or transitioned to, from another point in a given time t, due to limits on UGV acceleration, deceleration, and steering rate. Thus, not all maneuvers are physically realizable. Knowledge of the set of reachable maneuvers is important during navigation, since UGVs often have a limited amount of time to react to impending hazards.

A maneuver is defined as a transition between two arbitrary velocity-curvature pairs. A maneuver is characterized by an initial trajectory, $\tau_0=(\nu_0,\kappa_0)$, a final trajectory, $\tau_f=(\nu_f,\kappa_f)$, and a distance s over which the maneuver occurs and can be described by the quintuple $\chi=(\nu_0,\nu_f,\kappa_0,\kappa_f,s)$. A maneuver can thus be defined as:

Definition 7 (Maneuver): *A maneuver, χ, is a transition of any general shape from one location in the trajectory space $\tau_0=(\nu_0,\kappa_0)$ to another, $\tau_f=(\nu_f,\kappa_f)$ over a distance s.*

For a UGV with a location inside the trajectory space of (ν_0,κ_0), the maximum attainable velocity in time t is

$$\nu_{\text{reachable}}^{\max,\min} = \nu_0 \pm at, \qquad (21)$$

where a is the (assumed to be constant) acceleration/deceleration parameter. The maximum and minimum attainable curvatures for a front-steered vehicle in time t are

$$\kappa_{\text{reachable}}^{\max,\min}(\nu) = \kappa_0 \pm \dot{\kappa}_{\max}t, \qquad (22)$$

where $\dot{\kappa}_{\max}$ is the maximum rate of change of curvature, given as (see Figure 4)

$$|\dot{\kappa}_{\max}| = \frac{\tan \dot{\delta}_{\max}}{L}, \qquad (23)$$

where $\dot{\delta}_{\max}$ is the maximum steering rate of change and is assumed to be constant.

The reachable trajectory space, Λ, which describes a space of physically attainable maneuvers, can then be defined:

Definition 8 (Reachable Trajectory Space): *The reachable trajectory space, Λ, is the set of admissible velocity and curvature pairs a vehicle can transition to in a given time t from an initial location (ν_0,κ_0).*

The admissible trajectory can now be defined. An example is shown in Figure 11.

Definition 9 (Admissible Trajectory Space): *The admissible trajectory space, Θ, is the space of all dynamically admissible velocity and curvature pairs on a given terrain patch that can be transitioned to in a given time t from an initial location (ν_0,κ_0) given a vehicle's dynamic, steering, and drive train properties*:

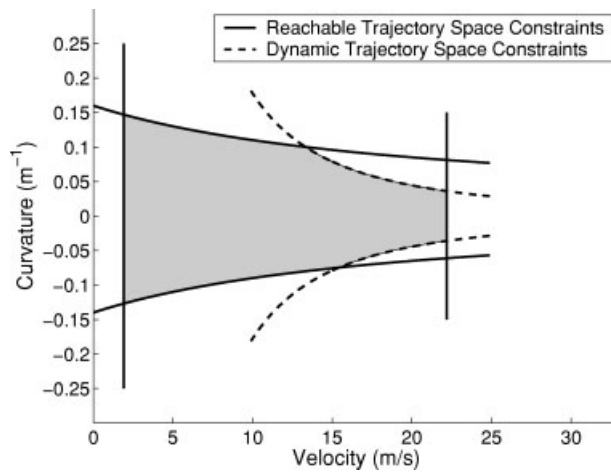$$\Theta = \Gamma \cap \Lambda. \qquad (24)$$

Figure 11. Admissible trajectory space for a HMMWV-class vehicle.

Figure 12. Nominal desired path with terrain patches.

3. HAZARD AVOIDANCE AND PATH RESUMPTION ALGORITHM DESCRIPTIONS

The trajectory space framework presented in Section 2 yields an instantaneous description of a UGV's mobility properties on a given terrain patch. During high speed navigation, however, a hazard avoidance algorithm must predicatively analyze mobility over terrain in front of the UGV. In this section, a hazard avoidance algorithm is presented that employs predictive analysis of UGV mobility over local terrain using the trajectory space framework presented in Section 2.

Consider a scenario similar to that illustrated in Figure 12. Here, a UGV attempts to follow a pre-planned nominal desired path, $x_{nominal}$, given by a high-level path planner. As discussed in Section 1.1, the nominal desired path has a corresponding nominal desired trajectory, $\tau_{nominal}$. An on-board forward-looking range sensor measures elevation and detects hazards in the local terrain region, which is divided into discrete patches. Calculation of the appropriate size and number of these patches is an important issue, but is not discussed here (Spenko, 2005). Note that by separating the terrain into patches, it is possible to account for the differences in terrain profile that will exist in the current sensor scan. In general, the size and number of terrain patches is related to the desired accuracy of the terrain inclination estimation used to compute 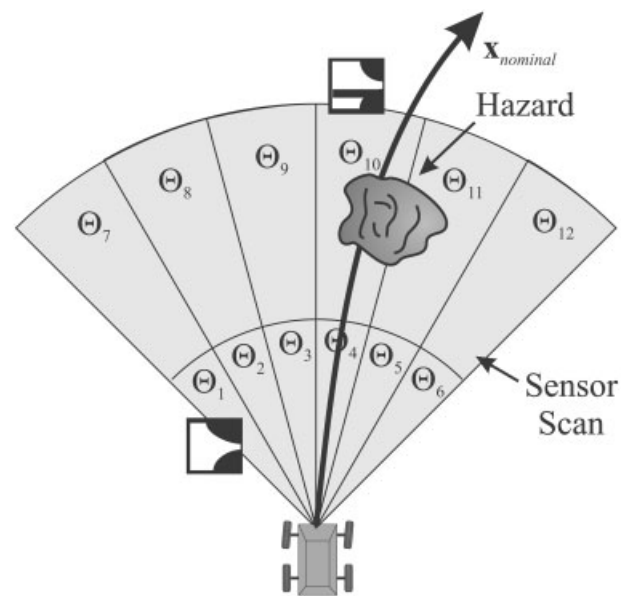the total admissible trajectory space. As the number of terrain patches increases, the estimated terrain roll and pitch for each patch becomes more accurate.

A hazard avoidance maneuver is enacted if either (or both) of two situations occurs: (1) A hazard lies on the vehicle's current desired path, $x_{nominal}$; 2) An element of $\tau_{nominal}$ whose corresponding path, $x_{nominal}$, lies in the ith terrain patch violates a trajectory space constraint corresponding to that patch. In other words, a UGV is commanded to follow a dynamically inadmissible trajectory.

At each sampling instant the hazard avoidance algorithm can be outlined as follows:

1. Acquire range sensor scan of surrounding terrain and discretize terrain into m patches;
2. compute trajectory space constraints [Eqs. (3), (5), (12), and (18)] of every terrain patch;
3. if a hazard lies on the vehicle's current desired path, $x_{nominal}$ or an element of $\tau_{nominal}$ whose corresponding path, $x_{nominal}$ lies in the ith terrain patch violates a trajectory space constraint corresponding to that patch, select a hazard avoidance maneuver;
4. compute a path resumption maneuver that will connect the end of the path generated by a hazard avoidance maneuver to the nominal desired path.
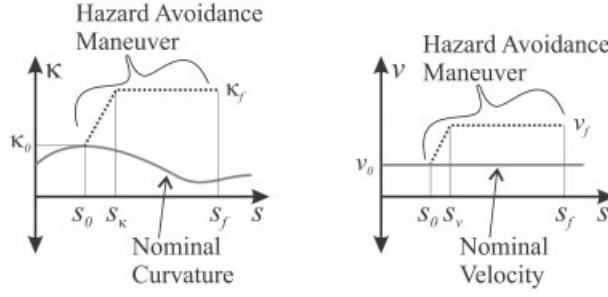
Figure 13. Hazard avoidance maneuver curvature (left) and velocity (right) profiles.

Step 1 is an important issue but is not a focus of this work. Step 2 has been described in Section 2. Steps 3 and 4 are described in the following sections.

3.1. Hazard Avoidance Maneuver Selection

Hazard avoidance maneuvers are dynamically admissible modifications of a UGV's nominal trajectory initiated by the presence of a hazard or dynamically unsafe trajectory. A hazard avoidance maneuver is a subset of the generalized maneuver described in Definition 7. It is composed of two segments that are truncated ramps of the highest possible slope. The first consists of a transition between the initial trajectory, $\tau_0 = (\nu_0, \kappa_0)$, and final trajectory, $\tau_f = (\nu_f, \kappa_f)$. The second consists of a constant velocity and curvature over a fixed distance (see Figure 13). The total length of the maneuver is $s = s_f - s_0$. Thus, the velocity profile of a hazard avoidance maneuver, χ_{h_ν}, can be described by

$$\chi_{h\_\nu} = \begin{cases} \nu_0 + \dfrac{d\nu}{ds}(s - s_0) & \text{for } s_0 < s \leqslant s_\nu, \\ \nu_f & \text{for } s_\nu < s \leqslant s_f. \end{cases} \quad (25)$$

The curvature profile of a hazard avoidance maneuver, χ_{h_κ}, can be described by

$$\chi_{h\_\kappa} = \begin{cases} \kappa_0 + \dfrac{d\kappa}{ds}(s - s_0) & \text{for } s_0 < s \leqslant s_k, \\ \kappa_f & \text{for } s_k < s \leqslant s_f, \end{cases} \quad (26)$$

where s_0 is the initial starting point of the maneuver, s_f is the final point of the maneuver, and s_ν and s_κ are given as

$$s_\nu = s_0 \pm \frac{\nu_f^2 - \nu_0^2}{2a}, \quad s_\kappa = s_0 \pm \bar{\nu}\left(\frac{\kappa_f - \kappa_0}{\dot{\kappa}_{\max}}\right), \quad (27)$$

where $\bar{\nu}$ is the average velocity over the time required to reach the final curvature.

When a hazardous situation is detected, an appropriate hazard avoidance maneuver must be selected. In this work, the selected maneuver must be dynamically admissible over all local terrain patches (and not just patches intersecting $\mathbf{x}_{\text{nominal}}$) to conservatively ensure maneuver safety.

For a terrain region that has been discretized into m patches, let Θ_j denote the admissible trajectory space for each terrain patch, $j \in [1, m]$. Let p be the number of hazards in the current sensor scan, and let H_k denote the hazard trajectory space for each hazard, $k \in [1, p]$. Then the total admissible trajectory space, Z, is defined as:

Definition 10 (Total Admissible Trajectory Space): *The total admissible trajectory space, Z, is the intersection of admissible trajectory spaces for every terrain patch minus the hazard trajectory space, H, for each hazard in the current sensor scan:*

$$Z \equiv (\Theta_1 \cap \ldots \cap \Theta_m) - H_1 - H_2 - \ldots - H_p. \quad (28)$$

The total admissible trajectory space is a representation of all safe dynamically admissible and reachable trajectories through a local terrain from the UGV's current position. The goal of the hazard avoidance algorithm is thus to find a maneuver, χ_h, such that $\tau_f = (\nu_f, \kappa_f) \in Z$. This maneuver transitions a UGV from a point in the total admissible trajectory space that violates a constraint to one that does not.

There are numerous techniques for finding τ_f that results in a "good" maneuver. Here, a simple and effective search-based method is proposed. In this approach, the trajectory space is discretized into closely spaced points. This discretized trajectory space is then treated as a graph, and τ_f is chosen as the point that minimizes the distance function Δ from the current point in the trajectory space, $\tau_0 = (\nu_0, \kappa_0)$, to a candidate point, $\tau_i = (\nu_i, \kappa_i)$:

$$\Delta = \sqrt{\frac{K_1}{\kappa_{max} - \kappa_{min}}(\kappa_0 - \kappa_i)^2 + \frac{K_2}{\nu_{max}}(\nu_0 - \nu_i)^2}, \quad (29)$$

where K_1 and K_2 are static positive gain factors. These factors affect the relative weighting of changes in velocity and curvature. A variety of search methods can be employed to find τ_f. In this work an exhaustive search was utilized due to the small size of the search space.

3.2. Path Resumption Maneuvers

After a hazard avoidance maneuver has been computed, a UGV must plan a kinematically and dynamically feasible path to return to the nominal desired path $x_{nominal}$. Here, an efficient path replanning algorithm is proposed to accomplish this. There are many approaches to this problem, and a more detailed analysis of the performance and convergence properties of the method along with a comparison with other techniques is described elsewhere (Spenko, 2005; Kelly & Nagy, 2003; Reuter, 1998).

Equations describing the motion of a front-steered vehicle can be written as

$$\kappa(t) = \tan(\delta(t))/L \quad \dot{\theta}(t) = \kappa(t)\nu(t),$$

$$\dot{x}(t) = \nu(t)\cos\theta(t) \quad \dot{y}(t) = \nu(t)\sin\theta(t), \quad (30)$$

where $\delta(t)$ is the steering input, $\theta(t)$ is the vehicle heading angle, $\nu(t)$ is the velocity input, and L is the vehicle wheelbase. If the curvature input is described as a function of time, $u(t)$, integration of Eq. (30) (with a change of variable from time to distance, and assuming constant velocity) yields

$$\kappa(s) = u(s), \quad \theta(s) = \nu\int_0^D \kappa(s)ds,$$

$$x(s) = \nu\int_0^D \cos\theta(s)ds, \quad y(s) = \nu\int_0^D \sin\theta(s)ds.$$
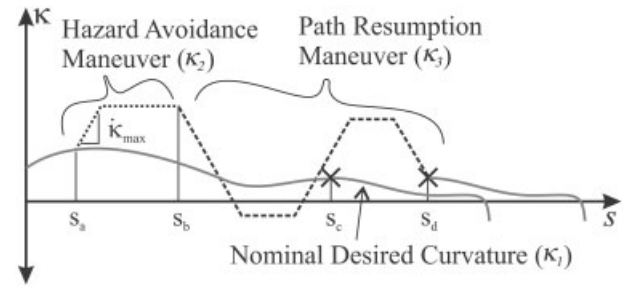
$$(31)$$

Figure 14. Curvature diagram for path resumption maneuver.

Consider the scenario illustrated by the plot shown in Figure 14. Here, the solid line represents a nominal trajectory's curvature as a function of distance. A hazard avoidance maneuver is executed at s_a, and the maneuver ends at s_b. The curvature profiles of the nominal desired path, hazard avoidance maneuver, and path resumption maneuver are defined as $\kappa_1(s)$, $\kappa_2(s)$, and $\kappa_3(s)$. These curvature profiles have associated heading and position profiles, $\theta(s)$, $x(s)$, and $y(s)$. The goal of the path resumption problem is to find $\kappa_3(s)$ in a computationally efficient manner (i.e., completed before the UGV has finished traversing the path generated by the hazard avoidance maneuver) such that the curvature, heading, and position at s_c is the same as at s_d:

$$(\kappa(s_c), \theta(s_c), x(s_c), y(s_c))_1 = (\kappa(s_d), \theta(s_d), x(s_d), y(s_d))_3,$$

$$(32)$$

where s_c is a desired "meeting point" of the replanning maneuver and the nominal trajectory, and s_d is the terminal point of the replanning maneuver. Clearly s_c and s_d need not be coincident.

A path resumption maneuver has the following properties:

- An initial curvature and velocity that is equal to the terminal curvature and velocity of a hazard avoidance maneuver, $(\nu(s_b), \kappa(s_b))_2 = (\nu(s_b), \kappa(s_b))_3$.
- A length s_r such that $s_r = s_d - s_b$.
- A trajectory profile such that $(\kappa(s_c), \theta(s_c), x(s_c), y(s_c))_1 = (\kappa(s_d), \theta(s_d), x(s_d), y(s_d))_3$.

The proposed path resumption method, here termed the "curvature matching method," is outlined as follows:

1. An initial choice of the location of the "meeting point," s_c, on the nominal trajectory is made. Here, s_c is initially chosen such that the path length of the path resumption maneuver is equal to the path length of the hazard avoidance maneuver:

$$s_c = 2s_b - s_a. \tag{33}$$

2. An initial value of s_d is chosen to be the smallest value such that a vehicle can transition from $\kappa_2(s_b)$ to $\kappa_3(s_d)$ without violating the vehicle's steering rate constraints:

$$s_d = \frac{\kappa_2(s_b) - \kappa_1(s_c)}{\nu \dot{\kappa}_{\max}}. \tag{34}$$

Steps 3–6 are designed to find a path resumption maneuver curvature profile, $\kappa_3(s)$, such that the following condition is satisfied:

$$\int_{s_a}^{s_c} \kappa_1(s)ds = \int_{s_a}^{s_b} \kappa_2(s)ds + \int_{s_b}^{s_d} \kappa_3(s)ds,$$

$$\tag{35}$$

$$\kappa_{\min} \leq \kappa_3(s) \leq \kappa_{\max},$$

where $\kappa_{\min}$ and $\kappa_{\max}$ are the minimum and maximum allowable curvatures given by the dynamic constraints of the total admissible trajectory space. Since $\kappa_{\min}$ and $\kappa_{\max}$ are included in this formulation, the curvature matching method is applicable for rough and rolling terrain because the cur-
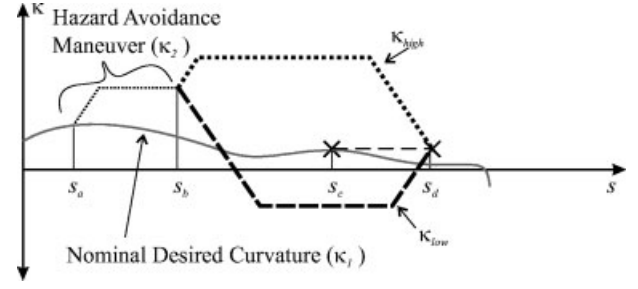
Figure 15. Illustration of curvature matching method constraints.

vature of the resulting path will not exceed the constraints generated by the trajectory space. Equation (35) states that the area under the hazard avoidance maneuver curvature profile plus the area under the path resumption maneuver curvature profile is equal to the area under the nominal desired trajectory curvature. This ensures that the heading angle at the end of the path resumption maneuver is identical to the heading angle of the nominal desired trajectory at the meeting point, $\theta_1(s_c) = \theta_3(s_d)$.

3. Two curvature constraints, κ_{high} and κ_{low}, for the path resumption maneuver are computed (see Figure 15). These constraints are defined as the maximum and minimum curvatures that transition the final curvature of the hazard avoidance maneuver, $\kappa_2(s_b)$, to the final curvature of the path resumption maneuver, $\kappa_3(s_d)$, given $\dot{\kappa} = \dot{\kappa}_{\max}$, $\kappa_{\text{high}} \leq \kappa_{\max}$, and $\kappa_{\text{low}} \geq \kappa_{\min}$. The area between the two constraints represents all possible curvatures that can transition $\kappa_2(s_b)$ to $\kappa_3(s_d)$. κ_{high} and κ_{low} are given as

$$\kappa_{\text{high}} = \begin{cases} \kappa(s_b) + \dfrac{d\kappa}{ds}s & \text{for } s_b < s \leq \dfrac{ds}{d\kappa}(\kappa_{\max} - \kappa(s_b)), \\[2mm] \kappa_{\max} & \text{for } \dfrac{ds}{d\kappa}(\kappa_{\max} - \kappa(s_b)) < s \leq \dfrac{ds}{d\kappa}(\kappa_{\max} - \kappa(s_d)), \\[2mm] \kappa_{\max} - \dfrac{d\kappa}{ds}s & \text{for } \dfrac{ds}{d\kappa}(\kappa_{\max} - \kappa(s_d)) < s \leq s_d, \end{cases} \tag{36}$$

$$\kappa_{\text{low}} = \begin{cases} \kappa(s_b) - \dfrac{d\kappa}{ds}s & \text{for } s_b < s \leq \dfrac{ds}{d\kappa}(\kappa_{\min} - \kappa(s_b)), \\[2ex] \kappa_{\min} & \text{for } \dfrac{ds}{d\kappa}(\kappa_{\min} - \kappa(s_b)) < s \leq \dfrac{ds}{d\kappa}(\kappa_{\min} - \kappa(s_d)), \\[2ex] \kappa_{\min} + \dfrac{d\kappa}{ds}s & \text{for } \dfrac{ds}{d\kappa}(\kappa_{\min} - \kappa(s_d)) < s \leq s_d. \end{cases} \tag{37}$$

In general, steps 4–6 generate a curvature profile that either follows the curvature constraints or transitions between them. These steps are described in detail; however, it is important to realize that the end result is simply a curvature profile that satisfies Eq. (35).

4. If the hazard avoidance maneuver has caused a UGV to deviate to the left of the desired nominal path, the path resumption maneuver generates a curvature profile that starts by following the lower curvature constraint, κ_{low}. This results in a path resumption maneuver that tends toward the right and is thus likely to minimize overall path deviation:

$$\kappa_3(s) = \begin{cases} \kappa_{\text{low}}(s) & \text{for } s_b < s \leq s_b + \Delta s, \\[2ex] \kappa_3(s - \Delta s) + \dfrac{ds}{v}\dot{\kappa}_{\max} & \text{for } s_b + \Delta s < s \leq s_d, \end{cases} \tag{38}$$

where Δs is the interval defined as

$$\Delta s = \frac{s_d - s_b}{n}, \tag{39}$$

where n is a fixed integer that represents the number of subdivisions of the curvature profile. If the UGV is on the right side of the nominal desired path, then the curvature profile begins by following the upper curvature constraint, κ_{high}. This results in a path resumption maneuver that tends toward the left:

$$\kappa_3(s) = \begin{cases} \kappa_{\text{high}}(s) & \text{for } s_b < s \leq s_b + \Delta s, \\[2ex] \kappa_3(s - \Delta s) - \dfrac{ds}{v}\dot{\kappa}_{\max} & \text{for } s_b + \Delta s < s \leq s_d. \end{cases} \tag{40}$$

5. If at any point the curvature profile of the path resumption maneuver is less than the lower curvature constraint, $\kappa_3(s) < \kappa_{\text{low}}(s)$, then the path resumption maneuver curvature is set equal to the lower curvature constraint, $\kappa_3(s) = \kappa_{\text{low}}(s)$. Similarly, if $\kappa_3(s) > \kappa_{\text{high}}(s)$ then the path resumption maneuver curvature is set equal to the upper cur-

vature constraint, $\kappa_3(s) = \kappa_{\text{high}}(s)$. This ensures the curvature profile does not violate the constraints imposed by the dynamic trajectory space and that the final curvature of the path resumption maneuver, $\kappa_3(s_d)$ is equal to the final curvature of the nominal path, $\kappa_1(s_c)$.

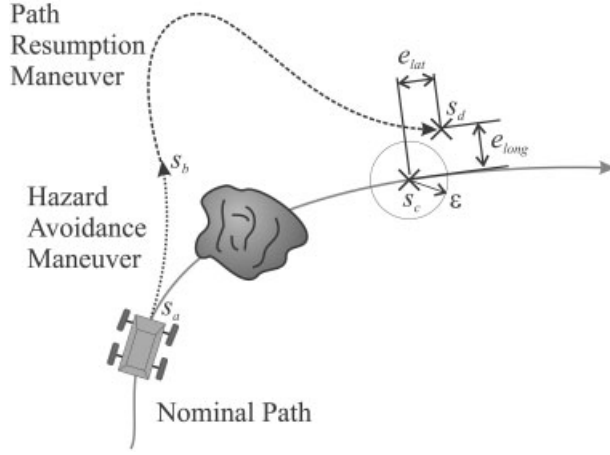6. If the area under the nominal desired trajectory's curvature profile is within a reasonable

Figure 16. Illustration of curvature matching method path.

tolerance, ε_κ, of the area under the hazard avoidance maneuver plus the path resumption maneuver curvature profiles:

$$\int_{s_a}^{s_c} \kappa_1(s)ds - \left(\int_{s_a}^{s_b} \kappa_2(s)ds + \int_{s_b}^{s_d} \kappa_3(s)ds \right) < \varepsilon_\kappa, \tag{41}$$

then the algorithm continues to step 7. Otherwise, Δs is increased and steps 4 and 5 are repeated. This iterative process searches the possible curvature profiles that constitute a path resumption maneuver while maintaining $\dot{\kappa} = \dot{\kappa}_{\max}$.

If the entire path resumption maneuver equals either κ_{high} or κ_{low} before Eq. (41) is satisfied, the distance for path resumption maneuver, s_d, is not large enough. In this case, Δs is reset to its original value, s_d is increased by a set length, and the algorithm returns to step 3.

From the path resumption maneuver curvature profile, heading and position profiles can be generated using Eq. (30). At this point, there is no guarantee that the position of the path resumption maneuver matches the nominal desired path (see Figure 16). If they do not match, s_c and s_d are

modified based on the Euclidian distance from $(x(s_c),y(s_c))_1$ to $(x(s_d),y(s_d))_3$.

7. An acceptable threshold for the final position error, ε, is defined. If the total position error, $e_{\text{total}} = \sqrt{(x_1(s_c)-x_3(s_d))^2+(y_1(s_c)-y_3(s_d))^2}$, lies within a circle of radius ε, then the algorithm is complete. If not, s_c and s_d are adjusted as

$$s_{c_{i+1}} = s_{c_i} - k_c(e_{\text{lon}}),$$

$$s_{d_{i+1}} = s_{d_i} - k_d(e_{\text{lat}}), \tag{42}$$

where k_c and k_d are static positive gains and e_{lon} and e_{lat} are the longitudinal and lateral error respectively and are given as

$$e_{\text{lat}} = (x_3(s_d) - x_1(s_c))\sin \theta_1(s_c)$$
$$+ (y_1(s_c) - y_3(s_d))\cos \theta_1(s_c), \tag{43}$$

$$e_{\text{lon}} = (x_1(s_c) - x_3(s_d))\cos \theta_1(s_c)$$
$$+ (y_1(s_c) - y_3(s_d))\sin \theta_1(s_c). \tag{44}$$

Due to the fact that the equations of motion are coupled and nonlinear [see Eq. (31)] algorithm convergence cannot be guaranteed. However, the convergence properties have been studied numerically and have yielded excellent results (Spenko, 2005). A ten thousand trial simulation using a PIII 1.5 GHz computer showed the curvature matching method generating a path with a median time of 10 ms and a mean time of 44 ms, which indicate the algorithm is sufficiently fast for use in high-speed situations.

Figure 17 shows an example path resumption maneuver generated using the curvature matching method. Note that the nominal path's curvature and heading and the path resumption curvature and heading profiles are identical at points s_c and s_d (upper left and upper right subplots), and points s_c and s_d are coincident along the path (lower subplot).

4. SIMULATION AND EXPERIMENTAL RESULTS

4.1. Experimental System Description

Experimental trials were conducted on the Autonomous Rough Terrain Experimental System
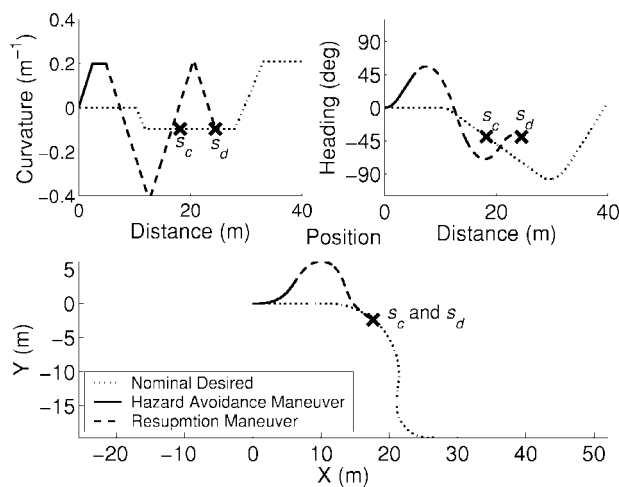
Figure 17. Example of curvature matching method.

(ARTEmiS); see Figure 18. ARTEmiS is a front-steer rear-wheel drive UGV that measures 0.88 m long, 0.61 m wide, and 0.38 m high. It has a 0.56 m wheelbase and 0.25 m diameter pneumatic tires. It is equipped with a 2.5 Hp Zenoah G2D70 gasoline engine, Crossbow AHRS-400 inertial navigation system, Novatel differential global positioning system capable of 0.2 m resolution (circular error probable), Futaba S5050 servos for steering, brakes, and throttle, and a PIII 700 MHz PC104 computer. ARTEmiS is not equipped with forward-looking range sensors. Instead, using knowledge of ARTEmiS' position, hazard locations are only revealed once they are within the range of a "virtual sensor." Simulations were conducted using a model of ARTEmiS and the commercial software package
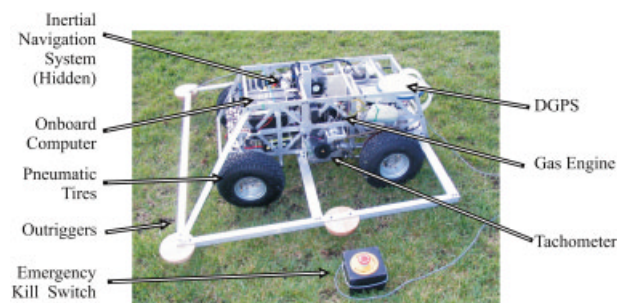
Figure 18. Diagram of ARTEmiS.

MSC.ADAMS/Car. The steering angle and throttle were controlled using a proportional-derivative control. For the steering angle, the gain was inversely proportional to the vehicle longitudinal velocity. Sufficient path following results were obtained using previously developed algorithms (Canudas de Wit, Siciliano & Bastin, 1996).

Because ARTEmiS exhibits only slight oversteer, for the purpose of the simulations and experiments presented in this chapter the steering constraints were considered to be derived from a neutral-steered vehicle. Also, note that the center of mass of ARTEmiS does not bisect the track width of the vehicle. Thus, the rollover constraints are not symmetric about zero curvature.

4.2. Validation of Hazard Avoidance Maneuver Algorithm

The hazard avoidance maneuver algorithm was validated through both simulation and experimental analysis. Over 80 h of experimental data were collected on a variety of terrain surfaces, profiles, and conditions, at speeds ranging from 3.0–9.0 m/s. This section provides results from five experiments.

For each experiment, ARTEmiS was placed in an initial starting location, (x_0, y_0), and commanded to follow a nominal desired trajectory, $\tau_{nominal}$, with a corresponding path, $\mathbf{x}_{nominal}$. Hazards consisted of traffic cones placed in various configurations. The range of the sensor varied among experiments from 12 m to 20 m (21 to 35 times the vehicle wheelbase). Other experiments were conducted to investigate the effects of a reduced sensor range on resulting hazard avoidance maneuvers. (Due to length constraints the results are not included here.) As expected, it was found that as the sensor range is reduced, the resulting hazard avoidance maneuvers are usually more severe and performed at lower-speeds than similar experiments conducted with longer-range sensors. Once a hazard was in range, it was assumed that the hazard geometry was known. All experiments used the curvature matching method to generate a path resumption maneuver. All experiments also used the maneuver selection cost function given in Eq. (29) with $K_1 < K_2$ unless otherwise noted.
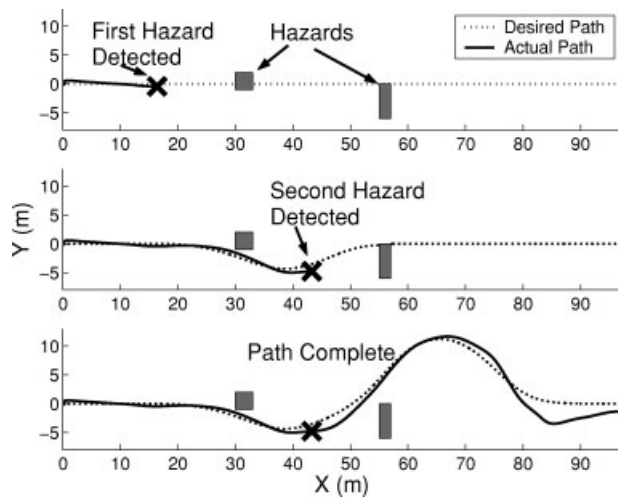
Figure 19. Hazard avoidance maneuvers executed for multiple hazards.

Figure 20. Trajectory space when the first hazard was detected.

4.3. Multiple Hazard Simulation and Experimental Results

Results from two experimental trials are presented that illustrate the ability of the algorithm to avoid multiple hazards. This section also contains simulation results for comparison to one of the experimental trials.

Figure 19 shows three "snapshot" subplots of the global positioning system (GPS) trace from an experiment for high-speed avoidance of two hazards. The experiment was performed on a field of mixed grass and dirt, at a desired velocity of 6.0 m/s. The nominal desired path was a 100 m long straight path. ARTEmiS detected the first hazard at $x = 16.4$ m. This is shown in the top subplot of Figure 19. At this point a hazard avoidance maneuver was executed. ARTEmiS followed the modified path until a second hazard was detected at $x = 43.2$ m. This is shown in the middle subplot of Figure 19. A second maneuver was then executed and ARTEmiS successfully resumed the nominal path, as shown in the lower section of Figure 19.

Figure 20 shows the trajectory spaces at the instant that the first hazard was detected. An **x** marks ARTEmiS' location in the trajectory space. Here, ARTEmiS modified its trajectory from $\tau_0 = (6.0, 0.00)$ to $\tau_f = (6.0, -0.03)$, i.e., it executed a sharp turn to avoid the hazard.
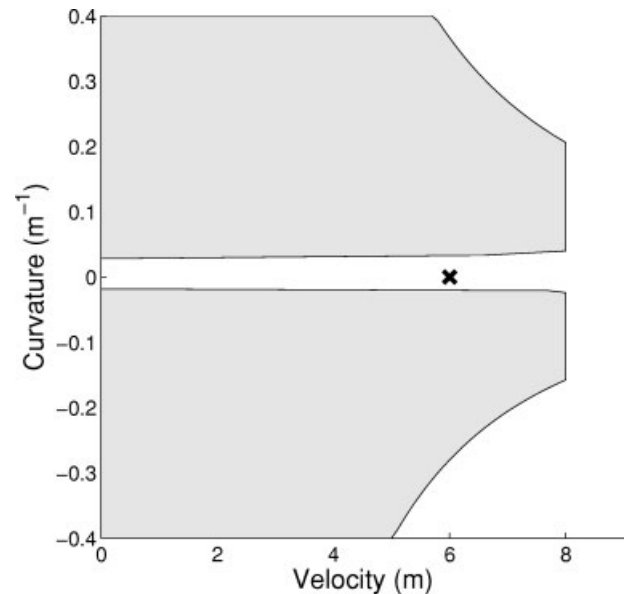
Figure 21 compares experimental and simulated GPS traces for these experiments. The top subplot displays the simulation results and the lower subplot shows the experimental results. The two results are quite similar, though the simulation generated a slightly different maneuver than the experimental system for the second hazard. This is due to differ-
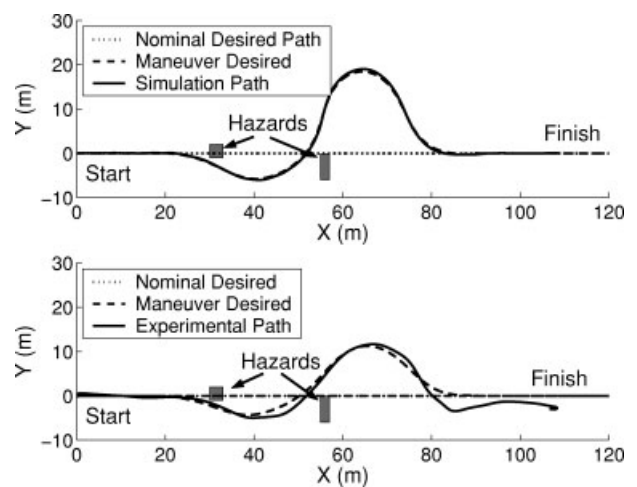

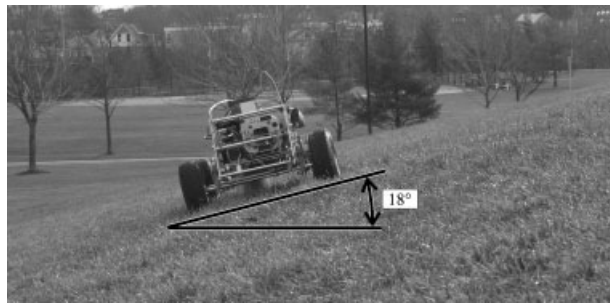**Figure 21.** Comparison of simulation (top) and experimental (bottom) results.

Figure 22. Image of ARTEmiS sloped terrain experiment.

Figure 23. Trajectory space comparison for flat and sloped terrain.

ences in ARTEmiS' position when the second hazard was identified. This can be attributed to position estimation and path tracking errors that are present in the experimental system.

Path tracking errors in the experimental system were due to position estimation errors and mechanical limitations of ARTEmiS's steering mechanism, which are backdrivable and slightly underpowered. Thus terrain roughness caused substantial disturbances to the steering system.

4.4. Sloped Terrain Experimental and Simulation Results

An important property of the hazard avoidance algorithm is its ability to account for the effects of terrain inclination. Here, the results of two experimental trials are compared. The experiments were identical except that the first was performed on flat terrain and the second was on terrain with a 15–18° slope with the fall line perpendicular to the initial direction of vehicle travel (see Figure 22).

The experiments were performed at a desired speed of 8.0 m/s. The nominal desired path for each trial was a 100 m long curved path. For both experiments ARTEmiS traversed the nominal desired path until it detected a hazard at $s=16.4$ m. At the time the hazard was identified, ARTEmiS selected a hazard avoidance maneuver of $\tau_f=(8.0, 0.12)$ on flat terrain. On sloped terrain ARTEmiS selected $\tau_f=(7.0, -0.06)$. This is due to the fact that on sloped terrain, $\tau_f=(8.0, 0.12)$ was not deemed to be a dynamically admissible maneuver due to the effects of terrain inclination. This can be seen in Figure 23.

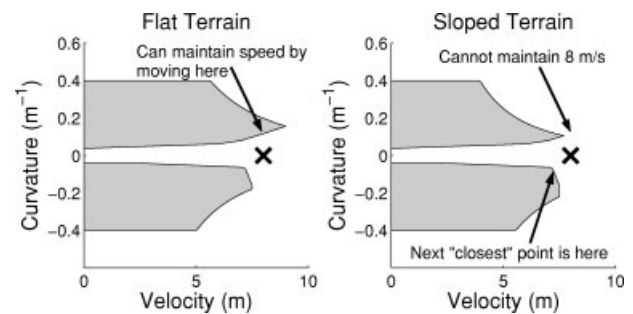GPS traces of the resulting paths are compared in Figure 24. There is significant path tracking over-

shoot in the flat terrain case due to steering servo rate limitations. However, this experiment illustrates the effect of terrain inclination on maneuver selection, and shows that the algorithm results in a dynamically admissible maneuver even on steeply sloped terrain.

4.5. Rough Terrain Experimental Results

Experiments on rough terrain were performed at Minute Man National Historic Park. The terrain consisted of a bumpy, uncut grass field. Physical terrain features tended to be on the order of one-half the wheel radius. Figure 25 illustrates the roughness of
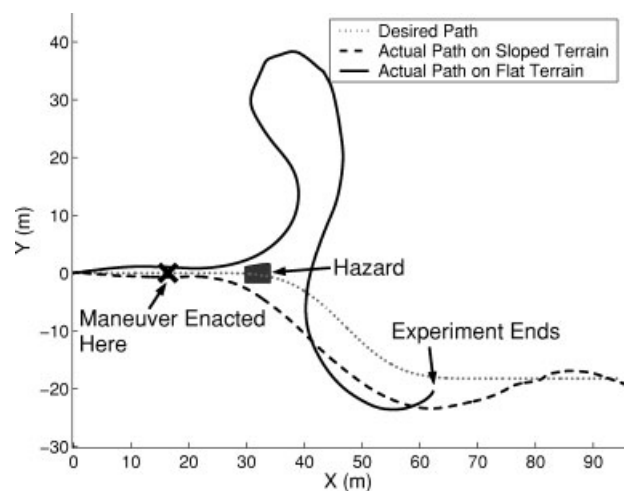

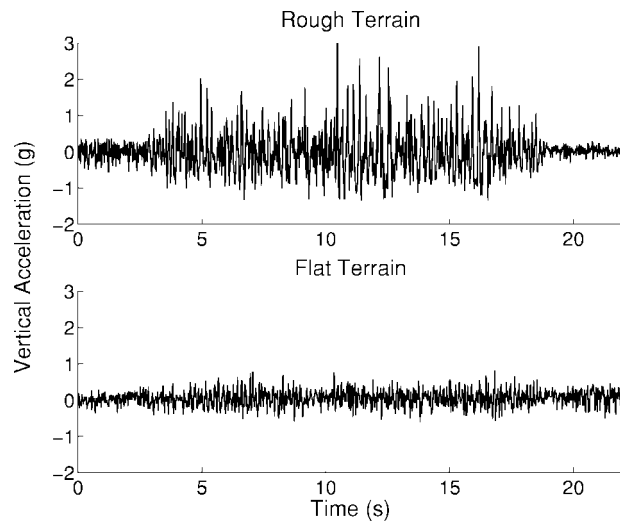**Figure 24.** Hazard avoidance maneuver enacted on flat and sloped terrain.

Figure 25. Vertical acceleration comparison on rough and flat terrain.

Figure 27. Rough terrain experimental results.

the terrain by comparing experimentally-measured UGV vertical acceleration measured on both smooth and rough terrain at the experiment site. Data were gathered while ARTEmiS traveled at 7 m/s.

Figure 26 shows the experimental site. The nominal desired path is a 100 m long straight path. ARTEmiS is pictured at the start of the path. The goal location is obstructed from view by the hazard. The hazard consists of a cluster of tall brushes, and small trees.
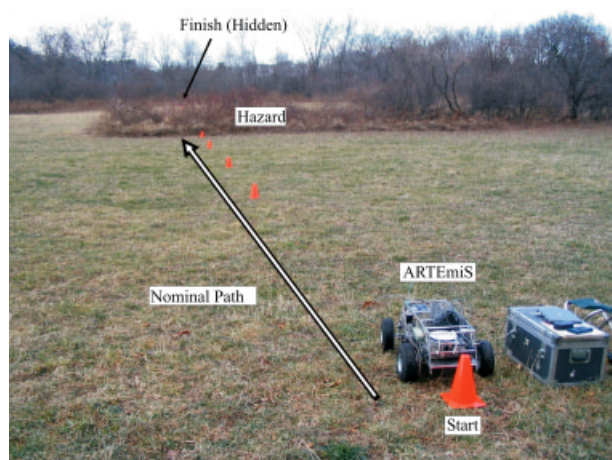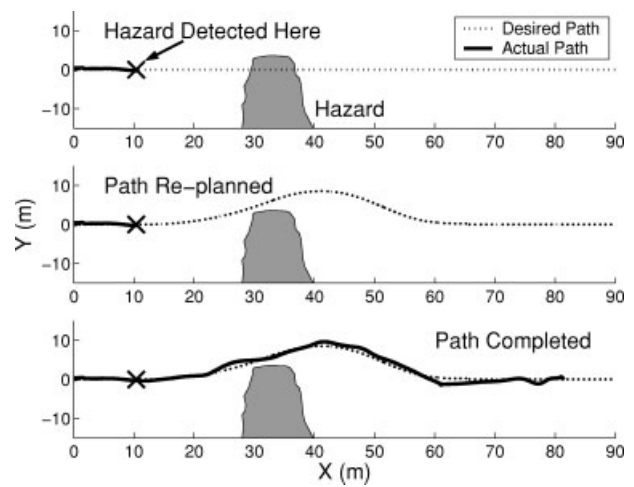
Figure 27 shows three "snapshot" subplots of the experiment. The experiment was performed at a speed of 7.0 m/s. ARTEmiS detected the first hazard at $x = 10.4$ m. This is shown in the top subplot of Figure 27. At this point, hazard avoidance and path resumption maneuvers were executed, as shown in the middle subplot of Figure 27. The lower section of Figure 27 shows the completed path.

Figure 28 shows the trajectory space at the time the hazard was detected. The dynamic rollover limits included an empirically determined "safety mar-
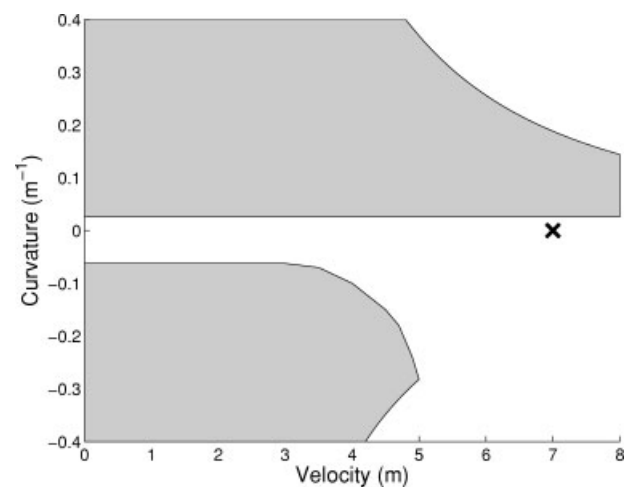

Figure 26. Rough terrain experimental setup.

Figure 28. Rough terrain trajectory space.

gin" to compensate for the effects of terrain roughness. When the hazard was detected, ARTEmiS modified its trajectory from $\tau_0 = (7.0, 0.00)$ to $\tau_f = (7.0, 0.03)$.

This experiment demonstrates that the proposed hazard avoidance algorithm can be applied in to UGVs operating at high speeds on rough terrain. These conditions are expected to be similar to actual operating conditions for many practical applications.

5. CONCLUSIONS

This paper has presented an algorithm for hazard avoidance for high-speed unmanned ground vehicles operating on rough, natural terrain. The algorithm accounts for dynamic effects, such as vehicle sideslip, rollover, and over/understeer, as well as vehicle steering dynamics, drive train properties, terrain geometry, and vehicle/terrain interaction. The method is computationally efficient (operating on the order of milliseconds), and thus suitable for on-board implementation. Extensive simulation and experimental results have been presented that demonstrate the algorithm's effectiveness. The hazard avoidance algorithm based on the trajectory space is only one of many that could be implemented, and future work focuses on expanding this area.

REFERENCES

Arakawa, K., & Krotkov, E. (1993). Fractal surface reconstruction for modeling natural terrain. Paper presented at the IEEE Conference on Computer Vision and Pattern Recognition, New York, NY.

Beer, F., & Johnston, E. (1988). Vector mechanics for engineers: Statics and dynamics. New York: McGraw–Hill.

Brock, O., & Khatib, O. (1999). High-speed navigation using the global dynamic window approach. Paper presented at the IEEE International Conference on Robotics and Automation, Detroit, MI.

Brooks, R.A. (1986). A robust layered control system for a mobile robot. IEEE J. Rob. Autom., 2(1), 14–23.

Canudas de Wit, C., Siciliano, B., & Bastin, G., eds. (1996). Theory of robot control. London: Springer-Verlag.

Chanclou, B., & Luciani, A. (1996). Global and local path planning in natural environment by physical modeling. Paper presented at the Intelligent Robots and Systems Conference, Osaka, Japan.

Chen, B.C., & Peng, H. (1999). Rollover warning of articulated vehicles based on a time-to-rollover metric. Paper presented at the ASME International Congress and Exposition, Knoxville, TN.

Coombs, D., Lacaze, A., Legowik, S., & Murphy, K. (2000). Driving autonomously off-road up to 35 km/h. Paper presented at the IEEE Intelligent Vehicle Symposium, Dearborn, MI.

Daily, M., Harris, J., Keirsey, D., Olin, K., Payton, D., Reiser, K., Rosenblatt, J., Tseng, D., and Wong, V. (1998). Autonomous cross-country navigation with the ALV. Paper presented at the IEEE International Conference on Robotics and Automation, Philadelphia, PA.

Fish, S. (2003, September). Overview of UGCV and PerceptOR status. Paper presented at the SPIE Unmanned Ground Vehicle Technology Conference, Orlando, FL.

Fox, D., Burgard, W., & Thrun, S. (1997). The dynamic window approach to collision avoidance. IEEE Rob. Autom. Mag., 4(1), 23–33.

Gerhart, G., Goetz, R., & Gorsich, D. (1999). Intelligent mobility for robotic vehicles in the army after next. Paper presented at the SPIE Unmanned Ground Vehicle Technology Conference, Orlando, FL.

Gillespie, T. (1992). Fundamentals of vehicle dynamics. Warrendale, PA: Society of Automotive Engineers.

Golda, D. (2003). Modeling and analysis of high-speed mobile robots operating on rough terrain. Unpublished M.S. thesis, Massachusetts Institute of Technology, Cambridge, MA.

Haddad, H., Khatib, M. Lacroix, S., & Chatila, R. (1998). Reactive navigation in outdoor environments using potential fields. Paper presented at the IEEE International Conference on Robotics and Automation, Leuven, Belgium.

Iagnemma, K., Kang, S., Brooks, C., & Dubowsky, S. (2003). Multisensor terrain estimation for planetary rovers. Paper presented at the Seventh International Symposium on Artificial Intelligence, Robotics, and Automation in Space, i-SAIRAS, Nara, Japan.

Kelly, A., & Nagy, B. (2003). Reactive nonholonomic trajectory generation via parametric optimal control. Int. J. Robot. Res., 22(7), 583–602.

Kelly, A., & Stentz, A. (1998). Rough terrain autonomous mobility—Part 2: An active vision, predictive control approach. Auton. Rob., 5, 163–198.

Langer, D., Rosenblatt, J.K., & Hebert, M. (1994). A behavior-based system for off-road navigation. IEEE Trans. Rob. Autom., 10(6), 776–783.

Manduchi, R., Castano, A., Talukder, A., & Matthies, L. (2005). Obstacle detection and terrain classification for autonomous off-road navigation. Auton. Rob., 18, 81–102.

Olin, K., & Tseng, D. (1991). Autonomous cross-country navigation: An integrated perception and planning system. IEEE Expert, 6(4), 16–30.

Philippsen, R., & Siegwart, R. (2003). Smooth and efficient obstacle avoidance for a tour guide robot. Paper presented at the IEEE International Conference on Robotics and Automation, Taipei, Taiwan.

Reuter, J. (1998). Mobile robot trajectories with continuously differentiable curvature: an optimal control approach. Paper presented at the IEEE/RSJ Conference on Intelligent Robots and Systems, Victoria, B.C., Canada.

Sanjiv, S., & Kelly, A. (1996). Robot planning in the space of feasible actions: Two examples. Paper presented at the IEEE International Conference on Robotics and Automation, Minneapolis, MN.

Shimoda, S., Kuroda, Y., & Iagnemma, K. (2005). Potential field navigation of high speed unmanned ground vehicles on uneven terrain. Paper presented at the IEEE International Conference on Robotics and Automation, Barcelona, Spain.

Shoemaker, C., & Borenstein, J. (2000). Overview and update of the Demo III experimental unmanned vehicle program. Paper presented at the SPIE Unmanned Ground Vehicle Technology, Orlando, Fl.

Simmons, R. (1996). The curvature-velocity method for local obstacle avoidance. Paper presented at the IEEE International Conference on Robotics and Automation, Minneapolis, MN.

Spenko, M. (2005). Hazard avoidance for high-speed rough-terrain unmanned ground vehicles. Unpublished Ph.D. thesis, Massachusetts Institute of Technology, Cambridge, MA.

Spenko, M., Iagnemma, K., & Dubowsky, S. (2004). High speed hazard avoidance for mobile robots in rough terrain. Paper presented in the SPIE Conference on Unmanned Ground Vehicles, Orlando, FL.

Walker, J. (2001). Unmanned ground combat vehicle contractors selected. DARPA News Release February 7, 2001.

White, F. (1994). Fluid mechanics. New York: McGraw–Hill.